Nanoscale piezoresponse studies of ferroelectric domains in epitaxial $BiFeO_3$ nanostructures

Seungbum Hong,[1,a)] Jeffrey A. Klug,[1,3] Moonkyu Park,[1,5] Alexandra Imre,[1,2] Michael J. Bedzyk,[1,3,4] Kwangsoo No,[5] Amanda Petford-Long,[1] and Orlando Auciello[1,2]
[1]*Materials Science Division, Argonne National Laboratory, 9700 South Cass Avenue, Lemont, Illinois 60439, USA*
[2]*Center for Nanoscale Materials, Argonne National Laboratory, Illinois 60439, USA*
[3]*Department of Physics and Astronomy, Northwestern University, Evanston, Illinois 60208, USA*
[4]*Materials Science Department and Materials Research Center, Northwestern University, Evanston, Illinois 60208, USA*
[5]*Department of Materials Science and Engineering, Korea Advanced Institute of Science and Technology, Yuseong-gu, Daejeon 305701 Republic of Korea*

(Received 16 July 2008; accepted 17 October 2008; published online 16 March 2009)

We report the dependence of the ferroelectric domain configuration and switching behavior on the shape (square versus round) of epitaxial $BiFeO_3$ (BFO) nanostructures. We fabricated (001) oriented BFO(120 nm)/$SrRuO_3$(SRO, 125 nm) film layers on (001) $SrTiO_3$ single crystals by rf magnetron sputter deposition, and patterned them to square (500×500 nm^2) and round (502 nm in diameter) shaped nanostructures by focused ion-beam lithography. The surface morphology and the crystalline structure of the nanostructures were characterized by scanning electron microscopy and x-ray diffraction, respectively, while the domain configuration was investigated using piezoelectric force microscopy. We found that the square-shaped nanostructures exhibit a single variant domain configuration aligned along the $[\bar{1}1\bar{1}]$ direction, whereas the round-shaped nanostructures exhibit seven variants of domain configuration along the $[\bar{1}1\bar{1}]$, $[1\bar{1}\bar{1}]$, $[11\bar{1}]$, $[111]$, $[\bar{1}11]$, $[1\bar{1}1]$, and $[\bar{1}\bar{1}1]$ directions. Moreover, local d_{33} piezoelectric coefficient measurements showed hysteresis loops with a strong displacement in the voltage axis (strong imprint) for the square-shaped nanostructures, while the round-shaped ones exhibited more symmetric loops. These findings have critical implications for the development of nanocapacitors for gigabyte to terabyte nonvolatile ferroelectric memories. © *2009 American Institute of Physics*. [DOI: 10.1063/1.3055412]

I. INTRODUCTION

There is currently much interest in magnetoelectric multiferroic materials, which exhibit both ferroelectric ordering and spontaneous magnetic ordering in a single phase.[1] The coexistence of and coupling between the ferroelectric and magnetic order parameters in such materials provide a rich platform for exciting research on new fundamental materials science and device physics. $BiFeO_3$ (BFO) is the most widely studied multiferroic as it is currently the only known multiferroic to exhibit ferroelectric and antiferromagnetic ordering at ambient temperatures.[2–4] BFO has a ferroelectric Curie temperature $T_C \sim 1100$ K and an antiferromagnetic Néel temperature $T_N \sim 640$ K, which are both well above room temperature. Furthermore, BFO is an environmentally benign ferroelectric with a large polarization (>100 $\mu C/cm^2$), which makes BFO an attractive candidate to replace lead-based [e.g., $Pb(Zr,Ti)O_3$] ferroelectric layers in device applications such as nonvolatile ferroelectric random access memories (FeRAMs).

With its robust ferroelectric state (high polarization and Curie temperature), BFO is an ideal candidate for memory applications, where it is imperative to reduce the size of the ferroelectric capacitors without losing polarization or thermal stability. However, the BFO-based capacitors suffer from a high coercive field of around 200 kV/cm, which needs to be reduced for low voltage operation of FeRAMs.[3] In addition, recent studies on BFO thin films revealed that it shows a strong imprint effect and that the imprint gets stronger as the thickness scales down.[5]

Based on the prior work mentioned above, we focused on understanding the conditions under which the nucleation barrier for opposite domain formation is low and symmetric. With that objective, we studied the dependence of the domain configuration and its switching behavior on the geometry of BFO nanostructures using piezoelectric force microscopy (PFM).

II. EXPERIMENTAL PROCEDURE

We used a multitarget magnetron sputter-deposition system to grow 125 nm thick (001) oriented $SrRuO_3$ (SRO) thin films on top of (001) $SrTiO_3$ (STO) single crystal substrate [MTI Corporation, miscut 0.5° from the (001) plane and 17° from the in-plane [010] directions]. This was followed by growth of (001)-oriented 120 nm thick BFO thin films on top of the SRO/STO substrate in an integrated deposition process without exposing the interfaces to air. The detailed deposition parameters for both SRO and BFO films are described in Table I.

[a)]Electronic mail: hong@anl.gov.

TABLE I. Deposition conditions for SRO and BFO film growths using rf magnetron sputter equipment.

Parameters	SRO	BFO
Power	51. W	51. W
Working pressure	11 mTorr	13 mTorr
Gas flow rate (Ar/O_2)	6 /4 SCCM	6 /4 SCCM
Deposition temperature	625 °C	650 °C

We characterized the crystallinity and the orientation of the films using x-ray diffraction (Huber 4 circle diffractometer) analysis. Both BFO and SRO layers were oriented with the pseudocubic (001) atomic planes in the film plane (Fig. 1). We determined the thickness of the SRO electrode layer from the oscillations in the scattered intensity along the 00*L* crystal truncation rod, and confirmed the thickness of the SRO and BFO layers via cross-section scanning electron microscopy (SEM) measurements. The thicknesses of the individual layers were 120 nm for BFO and 125 nm for SRO. The BFO film thickness is beyond the critical value (~30 nm) (Ref. 5) for a coherently strained film on STO. Accordingly, the BFO (001) Bragg peak (Fig. 1) is broadened due to strain relaxation.

We used focused ion-beam (FIB) lithography (FEI Nova 600 NanoLab, dual beam instrument) to fabricate the BFO-based nanostructures. The FIB system features a 30 kV Ga^+ ion beam with an 8.5 nm spot size, which was scanned multiple times to directly pattern the BFO layer. Figure 2 shows tilt-corrected plan-view SEM images of the pattern consisting of three square nanostructures (500×500 nm^2) and three round nanostructures (502 nm in diameter).

We conducted both vertical-PFM (V-PFM) and lateral-PFM (L-PFM) imaging, using a commercial atomic force

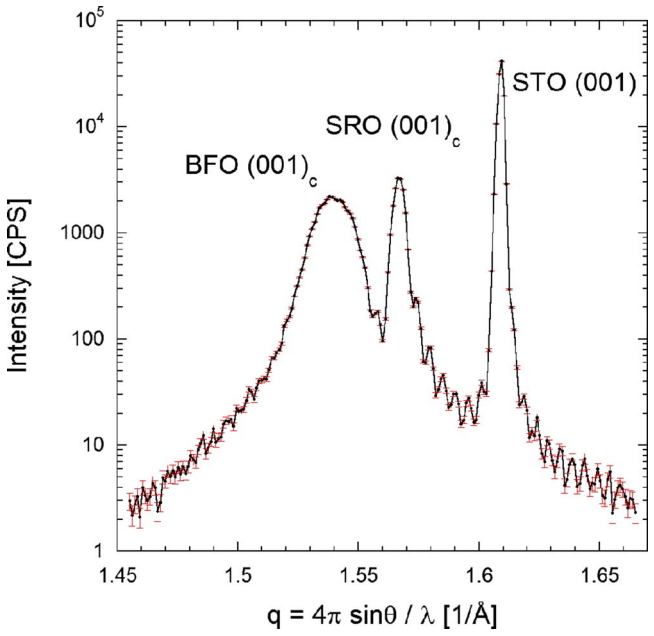

FIG. 1. (Color online) The x-ray scattered intensity from a specular crystal truncation rod scan through the (001) Bragg diffraction peaks of the BFO, SRO, and STO. The data were collected with horizontally and vertically focused Cu $K\alpha_1$ radiation from an 18 kW rotating anode source and a four-circle diffractometer.

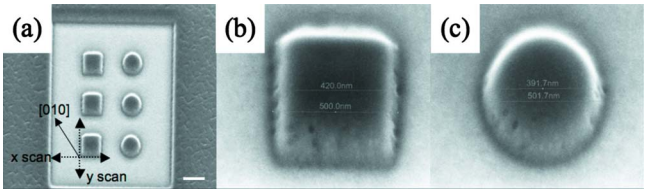

FIG. 2. (Color online) (a) SEM images of patterned nanostructures with AFM scan directions marked in relation to the [010] orientation of STO single crystal. (b) and (c) show magnified images of square- and round-shaped nanostructures in the first row. The white scale bar in (a) represents 500 nm.

microscope (AFM) (Asylum Research, MFP-3D) and lock-in amplifier (SR850, Stanford Research System).[7,8] To construct the full domain maps in three dimensions, we rotated the sample by 90° in *xy* plane and collected both V-PFM and L-PFM images.[9] Figure 2(a) shows the relationship between the AFM scan direction and the [010] crystal orientation of the STO single crystal substrate, where the [010] orientation has an angle of 33° with respect to *y*-scan direction. We applied an ac modulation voltage (3 V_{rms}, 17 kHz) to the Pt-coated Si tip (PPP EFM tips, Nanosensors, 2.6–3.0 N/m) while grounding the bottom SRO electrode. We collected local piezoelectric hysteresis loop at each specified point on the sample, using the same ac modulation voltage applied to the AFM tip (top electrode), while sweeping the dc voltage from −10 to 10 V to the bottom electrode.

III. RESULTS AND DISCUSSION

Figures 3 and 4 show the V- and L-PFM images of the square and round nanostructures for *x*- and *y*-scan directions (90° rotation in a counterclockwise direction), over a 1×1 μm^2 area. It is readily seen from the V-PFM image in Fig. 3 that the polarization in the square-shaped nanostructures is mostly oriented downward (bright phase with bright amplitude). The V-PFM image obtained after a 90° rotation implies that the amplitude and phase images are reproducible, and the dark contrast in the amplitude image, which rotated as well, indicates piezoelectrically inactive regions, most probably induced by the damage from Ga^+ ion impacts. The L-PFM images seen in Fig. 3 suggest that the dominant in-plane direction is along the *y*-axis of the coordinate system illustrated schematically in Fig. 5(b). By comparing the V- and L-PFM images and considering the crystal orientation of the substrate, one can identify the polarization direction, which is $[\bar{1}1\bar{1}]$ in this case [see Fig. 5(a)].

The round nanostructures showed much more complicated domain patterns, which need a more careful analysis than the square-shaped nanostructures. The V-PFM images seen in Fig. 4 show that the majority of the domains are oriented with polarization downward; however, a small portion of these domains exhibits polarization oriented upward. Analysis of phase images recorded across the area of the nanostructures indicated a ratio close to 6:4 for downward and upward polarized domains. L-PFM images with and without 90° rotation suggest that the downward domains are aligned along the $[\bar{1}1\bar{1}]$, $[1\bar{1}\bar{1}]$, and $[11\bar{1}]$ orientations,

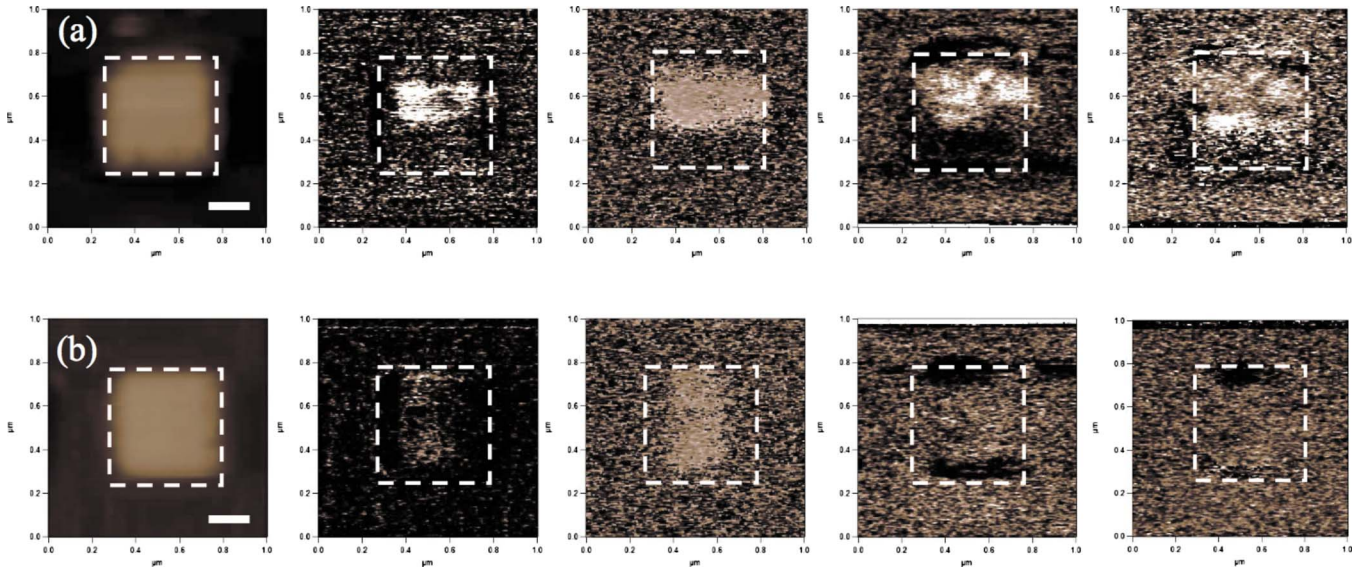

FIG. 3. (Color online) Topography, V-PFM (amplitude and phase), and L-PFM (amplitude and phase) (from left to right) images of nanostructures for (a) *x*- and (b) *y*-scan directions. The white bar in (a) and (b) represents the scale bar of 200 nm, and the white dotted lines are drawn only as eye guides to identify the pattern edges.

whereas the upward domains consist of all four polarization variants of [111], [1$\bar{1}$1], [$\bar{1}$11], and [$\bar{1}\bar{1}$1] directions, as shown in Figs. 5(c) and 5(d).

The reason that the square nanostructures contain single variant domain whereas the round nanostructures show seven variant domains is not completely clear at this stage. We believe that three factors play important roles in determining the equilibrium domain configurations, i.e., electric field concentration at edges and or corners, symmetry in strain field, and the potential formation of vortex domains. For the square nanostructures, the electrostatic boundary conditions are such that the corners may have a stronger electric field than the edges and central regions. Additionally the in-plane strain boundary conditions are more anisotropic. Both these factors can contribute to the lower symmetry of the domain configurations seen in the square nanostructures. The possibility of vortex domain formations cannot be excluded in the round capacitors, although close examination of in-plane polarization components indicates that the curl of polarization vectors does not go to 0, which should be the case for the vortex domains.[10]

We conducted local d_{33} hysteresis curve measurements at the center of both square- and round-shaped nanostructures, and the results are shown in Fig. 6. We were not able to reverse the polarization in the square-shaped nanostructures, such that the polarization direction remained parallel to [$\bar{1}\bar{1}\bar{1}$] during the voltage sweep from −10 to 10 V. The hysteresis loop recorded for the round nanostructure resembles a double loop, characteristic of antiferroelectric materials, but a close look at the zero voltage clearly indicates that there

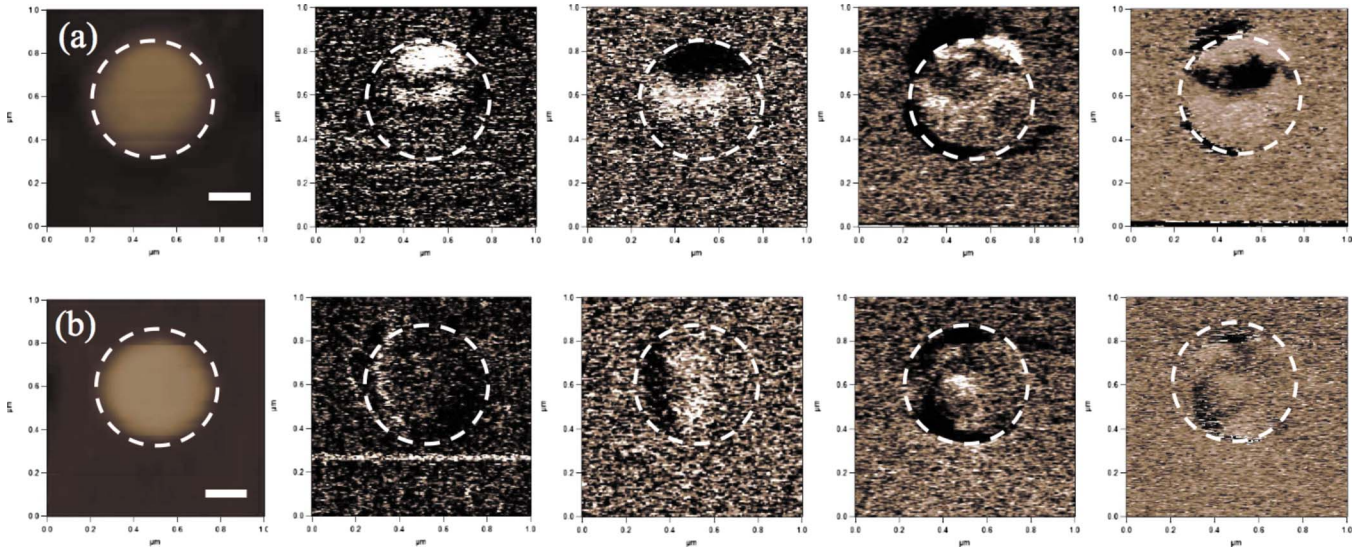

FIG. 4. (Color online) Topography, V-PFM (amplitude and phase), and L-PFM (amplitude and phase) (from left to right) images of nanostructures for (a) *x*- and (b) *y*-scan directions. The white bar represents the scale bar of 200 nm, and the white dotted lines are drawn only as eye guides to identify the pattern edges.

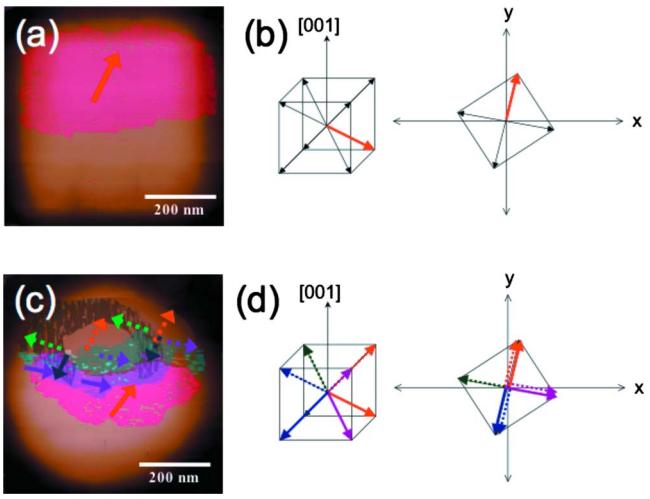

FIG. 5. (Color online) [(a) and (c)] Domain maps overlaid over topographies and [(b) and (d)] schematics of polarization directions with respect to the crystallographic orientations [(a) and (b)] for square-and [(c) and (d)] round-shaped nanostructures.

are two different remnant states depending on the history of voltage application. We were therefore able to pole the round-shaped nanostructure in either direction with a bias voltage of less than 10 V (5 V for positive domains and −8 V for negative domains).

We believe that the domain configurations of the square- and round-shaped nanostructures are responsible for their different switching behaviors. Square-shaped nanostructures showed a self-poled state with polarization oriented along the $[\bar{1}1\bar{1}]$ direction, which was manifested by the negative start point in the d_{33} hysteresis curve. A driving force other than the depolarization field (e.g., the strain field) maintained the polarization in this direction, resulting in an imprinted state between −10 and 10 V of electric bias to the sample. On the other hand, the round-shaped nanostructures, which contained multiple domains consisting of seven orientation variants, switched their polarization direction from upward to downward through domain nucleation and growth. We attribute the switchability and symmetry of the switching behavior in the round nanostructures to the presence of both upward and downward polarizations, which could facilitate switching of either direction due to easier domain nucleation.

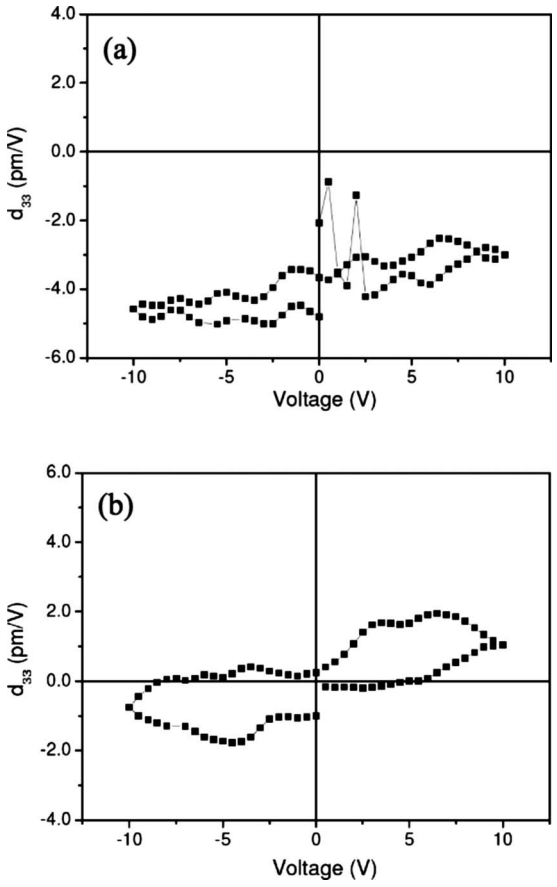

FIG. 6. Local d_{33} hysteresis curves of (a) square- and (b) round-shaped nanostructures.

One issue that should be further clarified is the extent of Ga^+ ion damage to the nanostructures and the extent to which the damaged area can influence both the domain configuration and its switching behavior. We annealed the patterned BFO film for 10 min at 650 °C in 1 Torr of O_2,[11] and found a significant recovery of the damaged area as shown in Fig. 7. Comparison between Figs. 7(a) and 7(b) clearly shows a recovery of a piezoelectrically inactive area. Furthermore, the overall amplitude of V-PFM and L-PFM images increased even in the piezoelectrically active area [see Figs. 7(a) and 7(b)], which implies that the surface damage was also recovered by the oxygen annealing. However, the domain analysis indicates that the prevailing polarization direction is still $[\bar{1}1\bar{1}]$, as it was prior to annealing. The amplitude images for the round-shaped nanostructures also showed a large amount of recovery in terms of piezoelectric active area (not shown here); however, the proportion of $[\bar{1}1\bar{1}]$ oriented polarization increased and the spatial distribution of each of the domain variants changed dramatically. More detailed studies are underway to study the effects of oxygen annealing on the domain configuration of BFO nanostructures, which may involve both changes in the local strain[12] and in the chemical environment,[13] leading to different equilibrium domain structures. We are also attempting to fabricate nanostructures using AFM-based nanolithography with diamond tips to avoid the ion bombardment damage characteristic of the FIB fabrication process.

IV. CONCLUSION

We have fabricated square (500×500 nm^2) and round (502 nm in diameter) nanostructures involving BFO/SRO (bottom electrode) layers grown via rf magnetron sputter deposition and FIB lithography to investigate the dependence of domain configuration and polarization reversal behavior on nanostructure shape (square versus circular). The PFM images suggest that nanostructures with a square shape have a single domain configuration, whereas the round nanostructures exhibit a configuration with seven domain variants. We attribute the more symmetric hysteresis loop and lower coercive field of the round nanostructures to the multidomain states, which facilitate domain nucleation and growth with vertical polarization component oriented in either upward or downward direction. Work underway will provide valuable

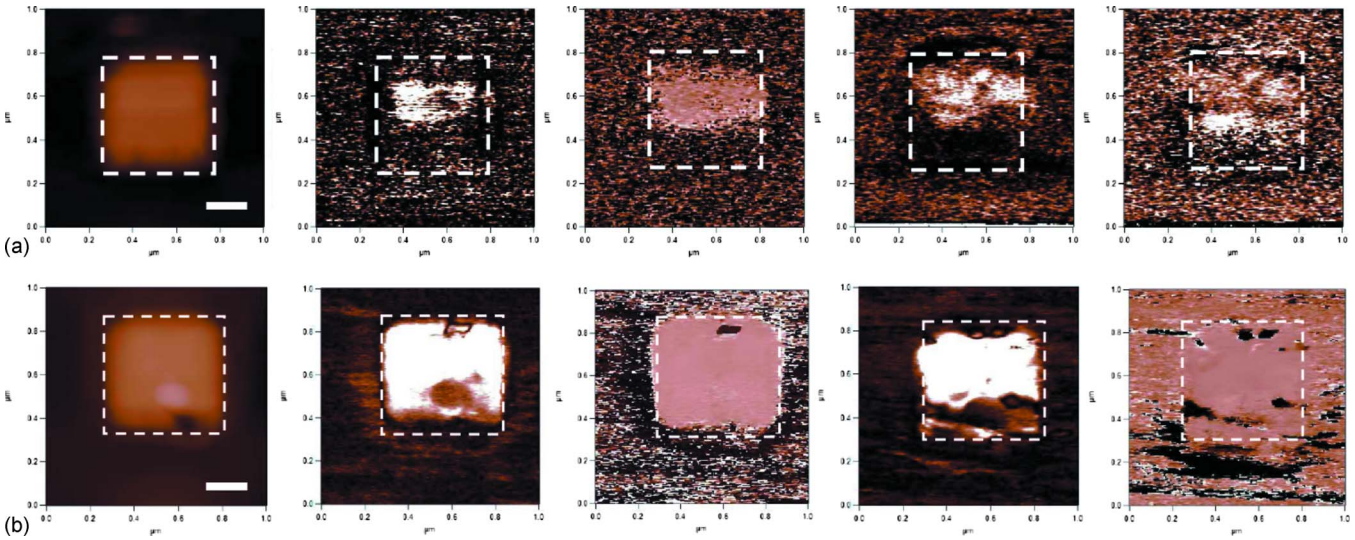

FIG. 7. (Color online) Topography, V-PFM (amplitude and phase), and L-PFM (amplitude and phase) (from left to right) (a) before and (b) after annealing (*x*-scan images). The white bar represents the scale bar of 200 nm, and the white dotted lines are drawn only as eye guides to identify the pattern edges.

information on the effect of annealing of the nanostructures on the polarization domain configuration and switching.

ACKNOWLEDGMENTS

The submitted manuscript has been created by UChicago Argonne, LLC, Operator of Argonne National Laboratory ("Argonne"). Argonne, a U.S. Department of Energy Office of Science laboratory, is operated under Contract No. DE-AC02-06CH11357. The U.S. Government retains for itself, and others acting on its behalf, a paid-up nonexclusive irrevocable worldwide license in said article to reproduce, prepare derivative works, distribute copies to the public, and perform publicly and display publicly, by or on behalf of the Government. The FIB nanofabrication was done at the Center for Nanoscale Materials User Facility that is supported by the U.S. Department of Energy, Office of Science, Office of Basic Energy Sciences, under Contract No. DE-AC02–06CH11357. The X-ray diffraction facility at NU is supported by MRSEC Grant No. DMR-0520513 from the National Science Foundation. The authors gratefully acknowledge the discussion on the manuscript with D. Fong, M. Pan, and R. Nath at Argonne National Laboratory.

[1]R. Ramesh and N. A. Spaldin, Nature Mater. **6**, 21 (2007).
[2]Y. H. Chu, M. P. Cruz, C. H. Yang, L. W. Martin, P. L. Yang, J. X. Zhang, K. Lee, P. Yu, L. Q. Chen, and R. Ramesh, Adv. Mater. (Weinheim, Ger.) **19**, 2662 (2007).
[3]S. Y. Yang, F. Zavaliche, L. Mohaddes-Ardabili, V. Vaithyanathan, D. G. Schlom, Y. J. Lee, Y. H. Chu, M. P. Cruz, Q. Zhan, T. Zhao, and R. Ramesh, Appl. Phys. Lett. **87**, 102903 (2005).
[4]S. V. Kalinin, M. R. Suchomel, P. K. Davies, and D. A. Bonnell, J. Am. Ceram. Soc. **85**, 3011 (2002).
[5]Y. H. Chu, T. Zhao, M. P. Cruz, Q. Zhan, P. L. Yang, L. W. Martin, M. Hujiben, C. H. Yang, F. Zavaliche, H. Zheng, and R. Ramesh, Appl. Phys. Lett. **90**, 252906 (2007).
[6]H. W. Jang, S. H. Baek, D. Ortiz, C. M. Folkman, C. B. Eom, Y. H. Chu, P. Shafer, R. Ramesh, V. Vaithyanathan, and D. G. Schlom, Appl. Phys. Lett. **92**, 062910 (2008).
[7]A. Roelofs, K. Szot, and R. Waser, in *Nanoscale Phenomena in Ferroelectric Thin Films*, edited by S. Hong (Kluwer, Boston, 2004), Chap. 6.
[8]S. Hong, J. Woo, H. Shin, J.-U. Jeon, Y. E. Pak, E. L. Colla, N. Setter, E. Kim, and K. No, J. Appl. Phys. **89**, 1377 (2001).
[9]S. V. Kalinin, B. J. Rodriguez, S. Jesse, J. Shin, A. P. Baddorf, P. Gupta, H. Jain, D. B. Williams, and A. Gruverman, Microsc. Microanal. **12**, 206 (2006).
[10]A. Gruverman, D. Wu, H.-J. Fan, I. Vrejoiu, M. Alexe, R. J. Harrison, and J. F. Scott, J. Phys.: Condens. Matter **20**, 342201 (2008).
[11]M. M. Saad, R. M. Bowman, and J. M. Gregg, Appl. Phys. Lett. **84**, 1159 (2004).
[12]A. Gruverman, B. J. Rodriguez, A. I. Kingon, R. J. Nemanich, J. S. Cross, and M. Tsukada, Appl. Phys. Lett. **83**, 728 (2003).
[13]J. A. Eastman, D. D. Fong, P. H. Fuoss, F. Jiang, G. B. Stephenson, S. K. Streiffer, R. V. Wang, K. Latifi, and C. Thompson, Abstr. Pap. - Am. Chem. Soc. **230**, U2794 (2005).